Geophysical Prospecting EAGE EUROPEAN ASSOCIATION OF GEOSCIENTISTS & ENGINEERS

Geophysical Prospecting, 2015, **63**, 1033–1049 doi: 10.1111/1365-2478.12221

Point-spread functions for interferometric imaging

Joost van der Neut and Kees Wapenaar

Department of Geoscience and Engineering, Delft University of Technology, Stevinweg 1, 2628 CN Delft, The Netherlands

Received August 2013, revision accepted May 2014

ABSTRACT

Interferometric redatuming is a data-driven method to transform seismic responses with sources at one level and receivers at a deeper level into virtual reflection data with both sources and receivers at the deeper level. Although this method has traditionally been applied by cross-correlation, accurate redatuming through a heterogeneous overburden requires solving a multidimensional deconvolution problem. Input data can be obtained either by direct observation (for instance in a horizontal borehole), by modelling or by a novel iterative scheme that is currently being developed. The output of interferometric redatuming can be used for imaging below the redatuming level, resulting in a so-called interferometric image. Internal multiples from above the redatuming level are eliminated during this process. In the past, we introduced point-spread functions for interferometric redatuming by cross-correlation. These point-spread functions quantify distortions in the redatumed data, caused by internal multiple reflections in the overburden. In this paper, we define point-spread functions for interferometric imaging to quantify these distortions in the image domain. These point-spread functions are similar to conventional resolution functions for seismic migration but they contain additional information on the internal multiples in the overburden and they are partly data-driven. We show how these point-spread functions can be visualized to diagnose image defocusing and artefacts. Finally, we illustrate how point-spread functions can also be defined for interferometric imaging with passive noise sources in the subsurface or with simultaneous-source acquisition at the surface.

Key words: Seismic interferometry, Virtual source, Seismic imaging.

INTRODUCTION

Subsurface imaging, characterization and monitoring with seismic wavefields typically rely on the availability of a macro velocity model. Erroneous velocity information can result in mispositioning of seismic horizons and defocusing of a seismic image. If the upper section of the subsurface is strongly heterogeneous, transmitted wavefields can be severely distorted, posing major challenges for seismic data processing. Bakulin and Calvert (2006) overcame these problems by placing seismic receivers in a horizontal (or deviated) borehole below the major complexities in the subsurface. Although seismic sources are still physically located at the earth's surface, they can be redatumed to the receiver level, creating a virtual-source array at depth. Since the propagation response between the surface and the borehole is actually recorded, redatuming can be implemented accurately and without information on the propagation velocity between the surface and the borehole. In the last decade, several related data-driven redatuming methods have emerged in the geophysical literature, commonly referred to as interferometric (redatuming) methods (Schuster 2009). Typically, interferometric redatuming is based on a cross-correlation formalism (Wapenaar and Fokkema 2006). However, there are several assumptions made in the underlying derivations that are not always fulfilled in practice. Free-surface multiples and intrinsic losses

E-mail: j.r.vanderneut@tudelft.nl

are not accounted for (Wapenaar and Fokkema 2006) and their presence easily results in the occurrence of spurious arrivals (Draganov *et al.* 2010; Van der Neut 2012). Moreover, interferometric redatuming is typically applied with one-sided illumination (i.e., sources above the receivers only), whereas the original theory is based on omni-sided illumination (i.e., sources both above and below the receivers) (Wapenaar and Fokkema 2006). As shown by Snieder, Wapenaar and Larner (2006), this violation of the underlying theory can result in spurious arrivals, even for very simple configurations. Instead, interferometric redatuming can be applied by multidimensional deconvolution (Wapenaar *et al.* 2011), yielding several important benefits, which will be reviewed later in this paper.

An interesting feature of interferometric methods is that full wavefields, including all internal reverberations in the overburden, are addressed, unlike in conventional (model-driven) redatuming methods (Berryhill 1984). Recently, Broggini, Snieder and Wapenaar (2012) and Wapenaar, Broggini and Snieder (2012) showed how the downgoing and upgoing wavefields at a target level in the subsurface can be generated from surface seismic data with the help of a smooth subsurface background model and a novel iterative scheme. Alternatively, these responses can be estimated from an accurate velocity model that includes reflectors. The latter approach was chosen by Vasconcelos and Rickett (2013), who utilized the framework for interferometric redatuming by multidimensional deconvolution to obtain virtual source and receiver arrays (i.e., extended images) in the subsurface. Either observed, estimated or modelled data are suitable input for interferometric redatuming as described in this paper.

Redatumed data can be interpreted as if there were virtual sources and receivers at the redatuming level. When evaluated at zero time-lag and zero space-lag, these data can be interpreted as an image with accurate amplitudes at the redatuming level (Wapenaar *et al.* 2012a). By including non-zero space-lags, so-called extended images can be generated (Vasconcelos and Rickett 2013), being useful input for rock- and fluid-property estimation (De Bruin, Wapenaar and Berkhout 1990) or migration velocity analysis (Biondi 2010). A superior seismic image can theoretically be obtained by applying interferometric redatuming to each depth level in the subsurface. However, computing the full Green's function at each depth level is computationally very intensive. For this reason, we prefer to apply redatuming to a selected subsurface level and proceed with conventional imaging below this level. The combination of interferometric redatuming and imaging has been traditionally referred to as interferometric imaging and we have seen various applications of this concept in the past, see Schuster (2009) for an overview.

Van der Neut *et al.* (2011) defined an interferometric point-spread function for interferometric redatuming by cross-correlation, which can be interpreted as the radiation pattern of a virtual source. The interferometric point-spread function is closely related to the resolution function or migration point-spread function as commonly defined in seismic migration (Schuster and Hu 2000). However, whereas the migration point-spread function is model-driven and includes only direct wave propagation through the overburden, the interferometric point-spread function is data-driven and includes all complexities of the overburden, including internal reverberations.

So far, the point-spread functions for interferometric redatuming and migration have been studied independently. In this paper, we define a new point-spread function for the special case where interferometric redatuming and migration are integrated, allowing us to diagnose the consequences of virtual source defocusing and internal multiples directly in the image domain. We have divided the paper into 10 sections, including an introduction and conclusion section. In section 2, we show how virtual sources can be generated in a horizontal or deviated borehole by cross-correlation of up- and downgoing wavefields. Traditionally, we cross-correlate upgoing waves with downgoing waves, such that the generated virtual sources radiate downwards (Mehta *et al.* 2007). However, if the medium is sufficiently heterogeneous, we can also generate upward radiating virtual sources by cross-correlation of multiply reflected downgoing waves with upgoing waves (Van der Neut *et al.* 2011). This is illustrated with an example. In section 3, we highlight several limitations of correlation-based interferometric redatuming and we demonstrate how some of these limitations can be mitigated by multidimensional deconvolution. In section 4, we interpret this mitigation in terms of the point-spread function for interferometric redatuming that quantifies the temporal and spatial focus at a virtual source location. The point-spread function for interferometric redatuming is closely related to the point-spread function or resolution function as we find it in seismic migration (Schuster and Hu 2000), which is formally introduced in section 5. Similar relations between interferometry and migration have been pointed out by Thorbecke and Wapenaar (2007). In section 6, we define a new point-spread function for interferometric imaging, which is defined as the sequential application of interferometric redatuming to a downhole receiver array and migration of the redatumed data. This point-spread function can be visualized for diagnostic purposes, as we demonstrate

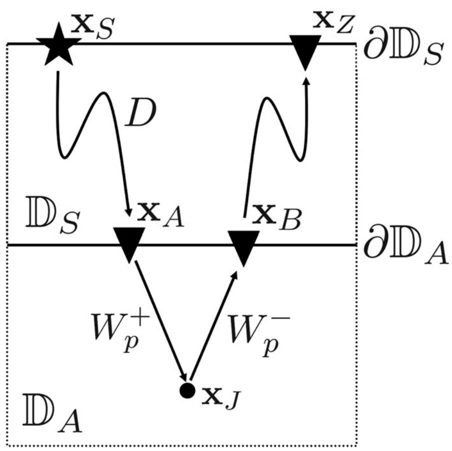

Figure 1 Configuration for interferometric redatuming and imaging. Sources are located at $\mathbf{x}_S$ at level $\partial\mathbb{D}_S$, above the overburden $\mathbb{D}_S$. Receivers and virtual sources are located at locations $\mathbf{x}_B$ and $\mathbf{x}_A$ at level $\partial\mathbb{D}_A$, above the target of our interest $\mathbb{D}_A$ (but below $\mathbb{D}_S$). Surface receivers at $\mathbf{x}_Z$ are not necessary for interferometric redatuming. Finally, $\mathbf{x}_J$ is an arbitrary location in the target area of our interest and $W_p^{\pm}$ are propagators for the primary wavefield.

in section 7. Finally, we define image-domain point-spread functions for two special applications. The first application is for a seismic survey with sources that act simultaneously at the surface. A common problem with simultaneous-source acquisition is posed by the cross-talk between individual sources. We show that the point-spread function as described in section 6 can be used to quantify this cross-talk in the image domain. The second application is passive seismic interferometry, where seismic signals are retrieved from ambient noise. We show that imperfections in the obtained results, stemming from non-uniform noise source distributions and mutual correlations between individual noise source signatures, can be diagnosed by our image-domain point-spread function.

INTERFEROMETRIC REDATUMING BY CROSS-CORRELATION

Consider the configuration shown in Fig. 1, where $\mathbf{x} = (x_1, x_2, x_3)^T$ is a spatial location with superscript T denoting transposition. In a conventional seismic experiment, sources and receivers are placed at locations $\mathbf{x}_S$ and $\mathbf{x}_Z$ at acquisition level $\partial\mathbb{D}_S$ (the earth's surface). To image, characterize or monitor the subsurface at a location $\mathbf{x}_J$ in the target zone, the source and receiver wavefields should be propagated through the overburden, being the medium between the acquisition level and the target. The velocity in the overburden is generally heterogeneous and should be known to allow accurate wavefield extrapolation.

Assume now that the receivers are not placed at level $\partial\mathbb{D}_S$ but in a horizontal borehole at level $\partial\mathbb{D}_A$, below the major complexities in the overburden. The overburden $\mathbb{D}_S$ is defined as the part of the medium that is located above $\partial\mathbb{D}_A$. The medium below $\partial\mathbb{D}_A$ is defined as $\mathbb{D}_A$. If a velocity model is available, source locations can be redatumed from $\partial\mathbb{D}_S$ to $\partial\mathbb{D}_A$ by downward continuation of the source wavefield (Berryhill 1984). However, since the propagation response between levels $\partial\mathbb{D}_S$ and $\partial\mathbb{D}_A$ is actually measured by the receivers in the borehole, redatuming can also be done without a velocity model. A range of different formulations have been presented for this purpose (Schuster and Zhou 2006), typically based on cross-correlation. Most of these formulations can be represented by the following expression in the frequency-space domain (indicated by the caret):

$$\hat{C}\left(\mathbf{x}_B, \mathbf{x}_A, \omega\right) = \int_{\partial\mathbb{D}_S} \hat{U}\left(\mathbf{x}_B, \mathbf{x}_S, \omega\right) \hat{D}^*\left(\mathbf{x}_A, \mathbf{x}_S, \omega\right) \mathrm{d}^2\mathbf{x}_S. \tag{1}$$

On the right-hand side, $\hat{U}\left(\mathbf{x}_B, \mathbf{x}_S, \omega\right)$ and $\hat{D}\left(\mathbf{x}_A, \mathbf{x}_S, \omega\right)$ are up- and downgoing wavefields recorded at receivers $\mathbf{x}_B$ and $\mathbf{x}_A$ from source $\mathbf{x}_S$. Further, superscript $*$ denotes complex conjugation and ω stands for the angular frequency. The integral is carried out over source locations on $\partial\mathbb{D}_S$. On the left-hand side, $\hat{C}\left(\mathbf{x}_B, \mathbf{x}_A, \omega\right)$ represents the correlation function, which is generally interpreted as the response to a source at $\mathbf{x}_A$ observed by a receiver at $\mathbf{x}_B$. Alternatively, interferometric redatuming can be applied in the $\tau - p$ domain, as shown by Tao and Sen (2013) and Ruigrok, Campman and Wapenaar (2011). Note that several assumptions have to be fulfilled for $\hat{C}$ to be an exact Green's function (Wapenaar 2006): free-surface multiples should be eliminated, the medium should be sufficiently heterogeneous to compensate for one-sided illumination and the medium should be lossless. Further, equation (1) is subject to a far-field high-frequency approximation (Wapenaar and Fokkema 2006). The latter can be circumvented by rewriting the integrand in equation (1) in terms of pseudo-differential operators (Zheng 2010).

Interferometric redatuming of decomposed fields is demonstrated with the following synthetic sub-salt imaging example. We use the acoustic Sigsbee 2B velocity model, as introduced by Paffenholz *et al.* (2002), inspired by the Sigsbee Escarpment Province in the Gulf of Mexico, see Fig. 2(a). In Fig. 2(b) we show an image that was obtained with one-way shot-profile migration from seismic data with monopole sources and receivers for pressure at the surface (Thorbecke, Wapenaar and Swinnen 2004). The imaging

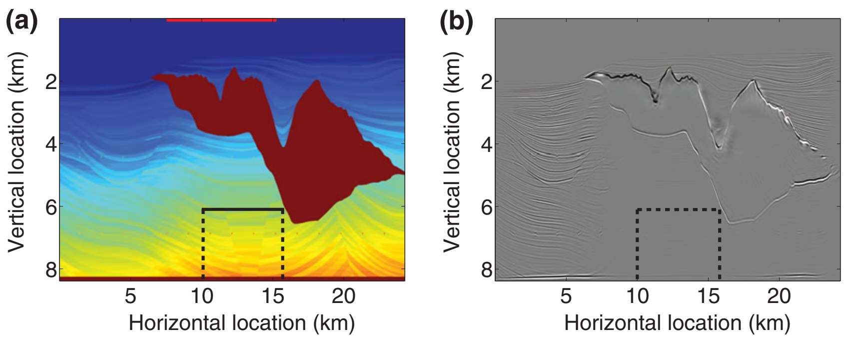

Figure 2 a) The Sigsbee 2B subsurface model. For imaging from the surface, sources and receivers cover the earth's surface over the complete length of the model. For interferometric imaging, the source and receiver arrays are indicated by red and black solid lines, respectively. b) Image obtained from surface seismic data. The black dashed square indicates the target area.

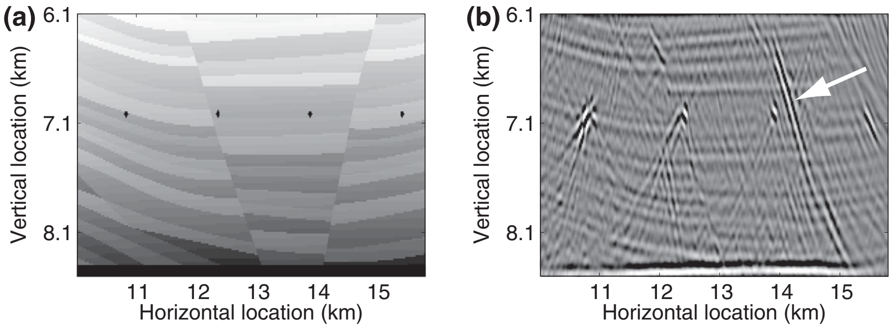

Figure 3 a) Local velocity model of the target area. b) Image of the target area obtained from physical sources and receivers at the surface. The white arrow indicates an artefact.

condition is based on deconvolution. We zoom in on a target area that is indicated by the dashed black lines. The medium inhomogeneities in the target area are shown in Fig. 3(a). In Fig. 3(b) we show the corresponding image, obtained from the surface data. Several artefacts can be identified, such as the one indicated by the white arrow. Such an event is related to internal scattering from the salt body, as pointed out by Thorbecke *et al.* (2004).

To generate physical downhole synthetic data, we change the acquisition geometry by placing 128 sources at the surface and 128 receivers in a horizontal borehole below the salt body, see Fig. 2(a). Gaussian noise has been added to the input data (with a signal-to-noise ratio of 5 dB). For several applications that are discussed below, it is critical to separate the wavefields into upgoing and downgoing constituents. In practice, it is often not so trivial to decompose the wavefields, which can severely limit the accuracy when interferometric redatuming is applied to field data, see Mehta *et al.* (2010) for examples. In this example, we decompose the wavefields by inversion, using sparsity promotion in the curvelet domain (Van der Neut and Herrmann 2013). It can be shown that the constructed correlation function $\hat{C}$ can be interpreted as a band-limited version of the Green's function with a virtual source emitting a downgoing field at $\mathbf{x}_A$ and a receiver sensing an upgoing field at $\mathbf{x}_B$ (Van der Neut *et al.* 2011). The response to these virtual sources can be used to image the target area below the receiver array in the borehole, indicated by the solid black line in Fig. 2(a). An image is obtained by applying the adjoint of the Born scattering operator to the redatumed data (Plessix and Mulder 2004), see Fig. 4(a). We observe that the resolution is lower than in Fig. 3(b). This is because the redatumed data contain the imprint of the auto-correlated source wavelet. If this wavelet is known, the image can be improved by deconvolution with the source auto-spectrum before imaging, see Fig. 4(b). Note that various artefacts that pollute Fig. 3(b) are not observed in Fig. 4(a,b). However, a different artefact is identified by the white arrow in Fig. 4(a), which is also a result from internal scattering from the salt flank. Finally, it should be emphasized that Fig. 3(b) depends on the velocity model of the overburden. Obtaining such a model is not trivial and errors in this model can severely distort the image. Contrary to that, the images in Fig. 4(a,b) are independent of velocity information above the borehole.

We can also generate virtual sources that radiate upwards. This is effectively achieved by interchanging the upgoing and downgoing fields in expression (1):

$$\hat{C}(\mathbf{x}_B, \mathbf{x}_A, \omega) = \int_{\partial \mathbb{D}_S} \hat{D}(\mathbf{x}_B, \mathbf{x}_S, \omega)\, \hat{U}^*(\mathbf{x}_A, \mathbf{x}_S, \omega)\, \mathrm{d}^2\mathbf{x}_S. \quad (2)$$

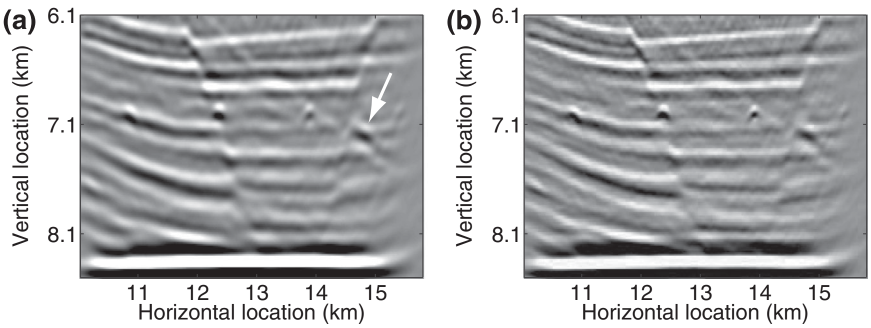

Figure 4 a) Image of the target area obtained from virtual source data by cross-correlation a) without and b) with source signature deconvolution. Virtual sources and receivers are located in the horizontal borehole at 6.1 km depth. Note the reference reflector at 8.3 km depth that can also be seen in Fig. 3(a).

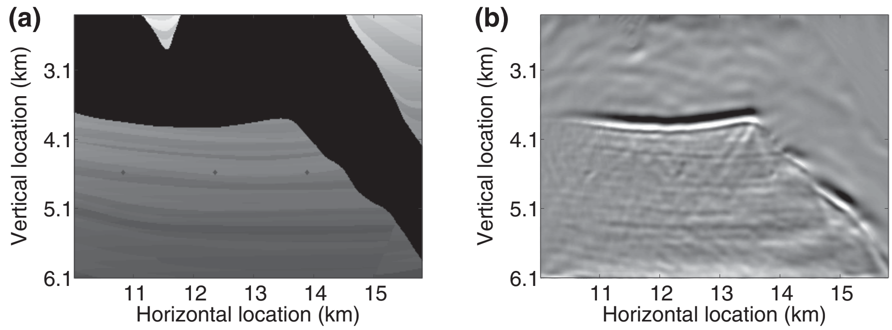

Figure 5 a) Local velocity model and b) image from virtual source data in a target area above the horizontal borehole. Virtual sources and receivers are located in the borehole at 6.1 km depth.

The causal part of the constructed correlation function $\hat{C}$ can now be interpreted as the response to a source emitting an upgoing field at $\mathbf{x}_A$, arriving as a downgoing field at $\mathbf{x}_B$ (Van der Neut *et al.* 2011). Note that the primary illumination, to create such a virtual source, comes from scattered wavefields and therefore the success of this method strongly depends on the heterogeneity of the medium below the receivers (Wapenaar 2006). Since the constructed virtual sources radiate upwards, they can be used for imaging the medium above the borehole. In Fig. 5(a) the true perturbations in a target area above the borehole in Fig. 2(a) are shown. Figure 5(b) shows an image from upward radiating virtual sources, illuminating the salt flank 'from below'. The salt flank, several layers and the point diffractors can be recognized. A similar concept was demonstrated by Vasconcelos, Snieder and Hornby (2008), using velocity-filtered fields in deviated boreholes. If surface seismic data are available, virtual sources that radiate upwards can also be constructed by combining the reflection responses at the surface with the downhole transmission response. This idea was proposed by Poliannikov (2011) and can be interpreted as a special application of source-receiver interferometry (Curtis and Halliday 2010). Poliannikov, Rodenay and Chen (2012) demonstrated how this methodology can be used to image a subducting crust from below.

Bakulin *et al.* (2007b) applied interferometric redatuming using receivers in horizontal boreholes for reservoir imaging and monitoring. Del Molino *et al.* (2011) applied a similar concept to remove ice-plate flexural noise from seismic data by redatuming sources from their actual locations on top of an ice plate in Alaska to receiver locations below the ice at the ocean floor. Interferometric redatuming can also be applied in vertical or deviated boreholes. By using diving waves or multiple scattering, steep targets can be illuminated under angles that are unseen in conventional processing. Willis *et al.* (2006) utilized this concept for imaging salt flanks. Similar studies were presented by Hornby and Yu (2007) and He *et al.* (2009). Others imaged steep dikes (Brand, Hurich and Deemer 2013) or faults (Chavarria *et al.* 2007) with virtual sources from vertical boreholes. If receivers $\mathbf{x}_A$ and $\mathbf{x}_B$ are located in different boreholes, interferometric redatuming results in so-called virtual crosswell data, which can be interpreted as the response to a virtual source in one borehole, observed by a receiver in the other borehole (Mehta *et al.* 2010). Byun, Yu and Seol (2010) generated virtual crosswell data from downhole receivers in horizontal boreholes for CO_2-sequestration monitoring. Interferometric redatuming has been applied to ocean-bottom cable (OBC) data to improve source repeatability in time-lapse experiments (Mehta *et al.* 2008). In this case, sources are redatumed from the water surface to receivers at the ocean floor. By exploiting multi-component measurements, virtual vertical and horizontal stress-sources can be generated at ocean-bottom receiver locations (Gaiser and Vasconcelos 2010). Similar concepts have been applied for generating virtual S-wave sources in boreholes from P-wave sources at the surface, see Bakulin *et al.* (2007a) and Gaiser *et al.* (2012) for applications. Finally, various authors have shown that equation (1) can be applied to surface data by choosing $\partial\mathbb{D}_A = \partial\mathbb{D}_S$. This approach turned out useful for interpolation of seismic wavefields. Wang, Luo and Schuster (2009) cross-correlated streamer data with observed Green's functions to interpolate near-offsets. Konstantaki *et al.* (2013) applied a similar idea to improve seismic imaging of scatterers in landfills. To suppress artefacts, it can be useful to use modelled Green's functions of well-known reflectors for the cross-correlation process, see Wang, Dong and Luo (2010) and Hanafy and Schuster (2014). For an overview of these and related applications, see Ramírez and Weglein (2009). Care should be taken, since most applications for surface data require the evaluation of incomplete source integrals. A potential way to handle such incompleteness is interpolation in the correlation gather, as suggested by Poliannikov and Willis (2011). Interferometric responses at the surface tend to be overwhelmed by surface waves (Forghani and Snieder 2010). This observation has led to numerous applications for surface-wave retrieval and subtraction of these retrieved waves from exploration data (Halliday *et al.* 2007).

INTERFEROMETRIC REDATUMING BY MULTIDIMENSIONAL DECONVOLUTION

For a variety of reasons, interferometric redatuming by cross-correlation does not always give an optimal result. It has already been mentioned that intrinsic losses should be negligible and that a far-field approximation be applied (Wapenaar and Fokkema 2006). Moreover, the free surface has not been accounted for and surface-related multiples should be removed prior to redatuming (Van der Neut 2012). Finally, the method is generally applied with one-sided illumination, which can be compensated only if the medium is sufficiently heterogeneous below the receiver level (Wapenaar 2006). Depending on the configuration, spurious events can populate the retrieved gathers (Snieder *et al.* 2006). Some non-physical arrivals can contain useful information, as has been demonstrated by various authors. Draganov *et al.* (2010) utilized such arrivals to estimate intrinsic attenuation. King, Curtis and Poole (2011) used them for velocity analysis. Dong, Sheng and Schuster (2006) and Mikesell *et al.* (2009) studied the virtual refraction, a spurious event that has later been used for downhole reservoir monitoring (Tatanova, Mehta and Kashtan 2009). King and Curtis (2012) convolved interferometric data with a Green's function to turn spurious events into physical events. A similar concept can be applied to virtual refractions to enhance first arrivals in seismic gathers (Bharadwaj *et al.* 2011).

Multidimensional deconvolution has been introduced as a tool to remove spurious events from the retrieved responses (Wapenaar *et al.* 2011) and to improve virtual source repeatability (Van der Neut 2012). This approach is based on a forward problem that can be represented in the frequency-space domain as:

$$\hat{U}(\mathbf{x}_B, \mathbf{x}_S, \omega) = \int_{\partial\mathbb{D}_A} \hat{G}_0(\mathbf{x}_B, \mathbf{x}_A, \omega)\, \hat{D}(\mathbf{x}_A, \mathbf{x}_S, \omega)\, \mathrm{d}^2\mathbf{x}_A. \tag{3}$$

Note that the integral in equation (3) is over the receiver array $\partial\mathbb{D}_A$, whereas the integral in equation (1) is over the source array $\partial\mathbb{D}_S$. The integrand contains the convolution of the unknown Green's function $\hat{G}_0$ and the downgoing field $\hat{D}$. The left-hand side contains the upgoing field $\hat{U}$. The unknown Green's function has to be retrieved from equation (3) by inversion. The retrieved Green's function $\hat{G}_0$ contains no contributions from the part of the medium above the receiver array. It is as if the virtual experiment were conducted in a medium with an infinite homogeneous half-space above the receiver level. This special property of $\hat{G}_0$ is well exploited in related applications for free-surface multiple elimination that are based on a similar formalism (Amundsen 2001).

Interferometric redatuming by multidimensional deconvolution involves the inversion of equation (3). This process should not be confused with interferometric redatuming by single-trace deconvolution, as presented by Vasconcelos and Snieder (2008). Although both processes enjoy various similar advantages, the underlying representations are essentially different. Interferometry by single-trace deconvolution is generally described as a summation process of deconvolved traces, whereas interferometry by multidimensional deconvolution is a multi-trace inversion process.

Since solving equation (3) is an ill-posed problem without a unique solution, we generally solve this problem either by least-squares inversion (Van der Neut *et al.* 2011), singular-value decomposition (Minato *et al.* 2011) or sparse inversion (Van der Neut and Herrmann 2013). We apply multidimensional deconvolution to the synthetic example that was discussed in the previous section. In Fig. 6, we show the migrated

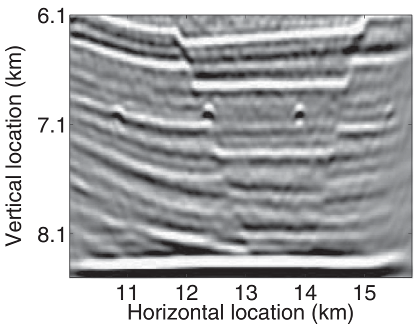

Figure 6 Image of the target area obtained from virtual source data by multidimensional deconvolution. Virtual sources and receivers are located in the horizontal borehole at 6.1 km depth. Note the reference reflector at 8.3 km depth that can also be seen in Fig. 3(a).

image that was obtained after interferometric redatuming by multidimensional deconvolution. We observe that the image is free of artefacts that stem from internal multiple reflections and that the resolution has improved to some extent.

A POINT-SPREAD FUNCTION FOR INTERFEROMETRIC REDATUMING

It can be shown theoretically that the least-squares solution of equation (3) obeys the normal equation (Menke 1989; Van der Neut *et al.* 2011) that can be written as:

$$\hat{C}(\mathbf{x}_B, \mathbf{x}'_A, \omega) = \int_{\partial\mathbb{D}_A} \hat{G}_0(\mathbf{x}_B, \mathbf{x}_A, \omega)\hat{\Gamma}_I(\mathbf{x}_A, \mathbf{x}'_A, \omega)\mathrm{d}^2\mathbf{x}_A, \tag{4}$$

where $\mathbf{x}'_A$ is introduced as another receiver location in array $\partial\mathbb{D}_A$ and subscript I stands for 'Interferometric'. The left-hand side contains the correlation function $\hat{C}$, as defined in equation (1), with $\mathbf{x}_A$ replaced by $\mathbf{x}'_A$. The right-hand side contains the interferometric point-spread function Γ_I that is defined as:

$$\hat{\Gamma}_I(\mathbf{x}_A, \mathbf{x}'_A, \omega) = \int_{\partial\mathbb{D}_S} \hat{D}(\mathbf{x}_A, \mathbf{x}_S, \omega)\hat{D}^*(\mathbf{x}'_A, \mathbf{x}_S, \omega)\mathrm{d}^2\mathbf{x}_S. \tag{5}$$

According to equation (4), the correlation function $\hat{C}$ can be interpreted as a multidimensional convolution of the desired Green's function $\hat{G}_0$ with the point-spread function $\hat{\Gamma}_I$. The point-spread function can be interpreted as the source function of the retrieved data, when interferometric redatuming is applied by cross-correlation. This is illustrated for the example that we discussed before. In Fig. 7(a), we show the point-spread function for a virtual source in the centre of the array. We observe clearly that the virtual source is focused at zero time-lag. However, we also observe several events at non-zero time-lags, due to free-surface and internal multiples in the downgoing wavefield. By inverting equation (4), we remove these internal multiples from the redatumed data. In Fig. 7(b), we show the point-spread function at the same virtual source location in the frequency-wavenumber domain. This representation can be interpreted as the radiation pattern of the virtual source, which can be used to diagnose virtual source defocusing.

A POINT-SPREAD FUNCTION FOR SEISMIC MIGRATION

Consider that we know the Green's function $\hat{G}_0\,(\mathbf{x}_B, \mathbf{x}_A, \omega)$ at level $\partial\mathbb{D}_A$. This Green's function can be interpreted by the following primary forward model (Wapenaar and Berkhout 1993):

$$\hat{G}_0\,(\mathbf{x}_B, \mathbf{x}_A, \omega) \approx \int_{\mathbb{D}_A} \hat{W}_p^-\,(\mathbf{x}_B, \mathbf{x}_J, \omega)\,\hat{R}\,(\mathbf{x}_J, \omega) \times \hat{W}_p^+\,(\mathbf{x}_J, \mathbf{x}_A, \omega)\,\mathrm{d}^3\mathbf{x}_J. \tag{6}$$

Here, $\hat{W}_p^+\,(\mathbf{x}_J, \mathbf{x}_A)$ and $\hat{W}_p^-\,(\mathbf{x}_B, \mathbf{x}_J)$ are downward (superscript $+$) and upward (superscript $-$) extrapolators of the primary (subscript p) wavefield from the virtual acquistion surface $\partial\mathbb{D}_A$ to potential reflection points $\mathbf{x}_J$ in the target area and vice versa. These operators can be computed from a background velocity model of the target area or from the reflection data itself, as in Common Focal Point (CFP) technology (Berkhout 1997; Thorbecke 1997). The reflection operator $\hat{R}\,(\mathbf{x}_J, \omega)$ characterizes the angle-dependent reflectivity at location $\mathbf{x}_J$ (De Bruin *et al.* 1990). The integral is carried out over volume $\mathbb{D}_A$ below the acquisition level $\partial\mathbb{D}_A$ (see Fig. 1).

Seismic migration can be interpreted as a double focusing operation followed by a summation over the range of available frequencies Ω. Following this interpretation, the migrated data M_G at location $\mathbf{x}'_J$ in the target area can be obtained as (Berkhout and Wapenaar 1993):

$$M_G\left(\mathbf{x}'_J\right) = \int_\Omega \int_{\partial\mathbb{D}_A} \int_{\partial\mathbb{D}_A} \{\hat{W}_p^+(\mathbf{x}'_J, \mathbf{x}_B, \omega)\}^* \hat{G}_0(\mathbf{x}_B, \mathbf{x}_A, \omega) \times \{\hat{W}_p^-(\mathbf{x}_A, \mathbf{x}'_J, \omega)\}^* \mathrm{d}^2\mathbf{x}_A \mathrm{d}^2\mathbf{x}_B \mathrm{d}\omega. \tag{7}$$

By substituting equation (6) into equation (7), it can be shown that migration yields a blurred image of the reflection operator:

$$M_G(\mathbf{x}'_J) \approx \int_\Omega \int_{\mathbb{D}_A} \hat{R}(\mathbf{x}_J, \omega)\hat{\Gamma}_M(\mathbf{x}_J, \mathbf{x}'_J, \omega)\mathrm{d}^3\mathbf{x}_J\, d\omega, \tag{8}$$

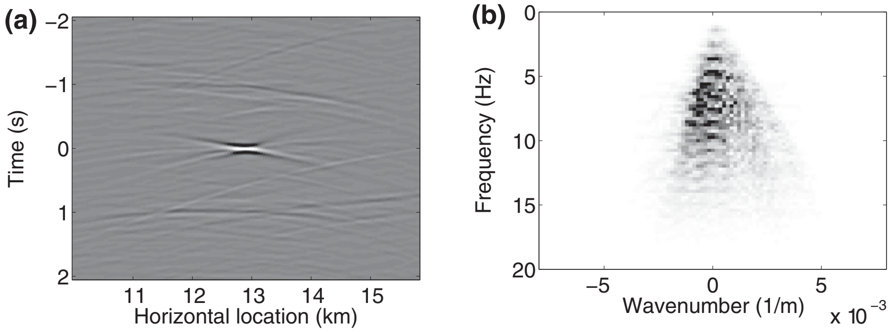

Figure 7 Point-spread function for a virtual source in the centre of the array $\partial\mathbb{D}_A$ in a) the time-space domain and b) the frequency-wavenumber domain.

where $\hat{\Gamma}_M(\mathbf{x}_J, \mathbf{x}'_J)$ is the migration point-spread function (Schuster and Hu 2000) (also known as the resolution function):

$$\hat{\Gamma}_M(\mathbf{x}_J, \mathbf{x}'_J, \omega) = \int_{\partial\mathbb{D}_A}\int_{\partial\mathbb{D}_A} \{\hat{W}_p^+(\mathbf{x}'_J, \mathbf{x}_B, \omega)\}^* \hat{W}_p^-(\mathbf{x}_B, \mathbf{x}_J, \omega) \times \hat{W}_p^+(\mathbf{x}_J, \mathbf{x}_A, \omega)\{\hat{W}_p^-(\mathbf{x}_A, \mathbf{x}'_J, \omega)\}^* \mathrm{d}^2\mathbf{x}_A \mathrm{d}^2\mathbf{x}_B. \quad (9)$$

Subscript M stands for 'Migration'. An image can also be obtained by inversion of the forward model. By doing that, we effectively deconvolve the migration point-spread function from the migrated data. This approach has been referred to as image restoration (Berkhout and Wapenaar 1993).

A POINT-SPREAD FUNCTION FOR INTERFEROMETRIC IMAGING

When interferometric redatuming and imaging are sequentially applied, we refer to the result as an interferometric image. In the following, we consider the case where the correlation function $\hat{C}(\mathbf{x}_B, \mathbf{x}_A, \omega)$ is retrieved by evaluation of equation (1) and interpreted as the reflection response as if there were a source at $\mathbf{x}_A$ and a receiver at $\mathbf{x}_B$. This correlation function is migrated in the target zone $\mathbb{D}_A$ (see Fig. 1). Analogous to equation (7), we interpret such a migrated image as:

$$M_C(\mathbf{x}'_J) = \int_\Omega\int_{\partial\mathbb{D}_A}\int_{\partial\mathbb{D}_A} \{\hat{W}_p^+(\mathbf{x}'_J, \mathbf{x}_B, \omega)\}^* \hat{C}(\mathbf{x}_B, \mathbf{x}'_A, \omega) \times \{\hat{W}_p^-(\mathbf{x}'_A, \mathbf{x}'_J, \omega)\}^* \mathrm{d}^2\mathbf{x}'_A \mathrm{d}^2\mathbf{x}_B \mathrm{d}\omega. \quad (10)$$

By substituting equations (4) and (6) into equation (10), it follows that:

$$M_C(\mathbf{x}'_J) \approx \int_\Omega\int_{\mathbb{D}_A} \hat{R}(\mathbf{x}_J, \omega)\hat{\Gamma}_{IM}(\mathbf{x}_J, \mathbf{x}'_J, \omega)\mathrm{d}^3\mathbf{x}_J \mathrm{d}\omega, \quad (11)$$

with

$$\hat{\Gamma}_{IM}(\mathbf{x}_J, \mathbf{x}'_J, \omega) = \int_{\partial\mathbb{D}_A}\int_{\partial\mathbb{D}_A} \{\hat{W}_p^+(\mathbf{x}'_J, \mathbf{x}_B, \omega)\}^* \hat{W}_p^-(\mathbf{x}_B, \mathbf{x}_J, \omega) \times \left[\int_{\partial\mathbb{D}_A} \hat{W}_p^+(\mathbf{x}_J, \mathbf{x}_A, \omega)\hat{\Gamma}_I(\mathbf{x}_A, \mathbf{x}'_A, \omega)\mathrm{d}^2\mathbf{x}_A\right] \times \{\hat{W}_p^-(\mathbf{x}'_A, \mathbf{x}'_J, \omega)\}^* \mathrm{d}^2\mathbf{x}'_A \mathrm{d}^2\mathbf{x}_B. \quad (12)$$

From equation (11) it can be concluded that the interferometric image is not blurred by $\hat{\Gamma}_M$ but by $\hat{\Gamma}_{IM}$, carrying an additional imprint of the interferometric point-spread function $\hat{\Gamma}_I$. We refer to $\hat{\Gamma}_{IM}$ as the interferometric migration point-spread function. This point-spread function can be used to diagnose the resolution of an interferometric image, as is illustrated in the following section.

ILLUMINATION DIAGNOSIS IN THE IMAGE DOMAIN

The theory that was derived in the previous section can be used for illumination diagnosis in the image domain. For illustrative purposes, we consider the synthetic Sigsbee model example that was discussed in the previous sections. In Fig. 4(a), we show an image of the target area that was obtained from cross-correlated data $\hat{C}$. To diagnose the interferometric migration point-spread function for this problem, a grid of point scatterers is added to a smooth version of the velocity model of the target area $\mathbb{D}_A$ below the receivers, see Fig. 8(a). These point scatterers represent trial image points. Our aim is to analyse the migration point-spread function and the interferometric migration point-spread function at these trial image points. First, we assume that physical sources are located in the borehole at the positions of the receivers. We compute Green's functions $\hat{G}_\delta(\mathbf{x}_B, \mathbf{x}_A, \omega)$ for the medium with point scatterers, where $\mathbf{x}_A$ and $\mathbf{x}_B$ are source and receiver locations

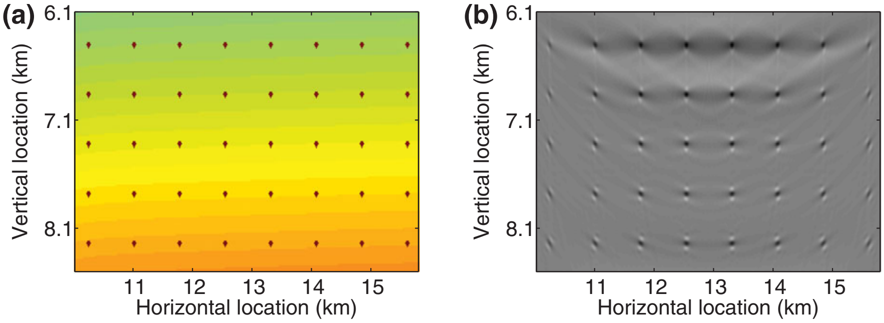

Figure 8 a) Background velocity model of the target area with an additional grid of point scatterers. b) Image of the point scatterers obtained with physical sources in the horizontal borehole.

in the borehole. In practice, the Green's function is replaced by a band-limited version $\hat{P}_\delta = \hat{S}\hat{G}_\delta$, where $\hat{S}$ is the Fourier transform of a wavelet. We assume that the reflectivity of the background medium with point scatterers can be described as a superposition of delta functions, where absolute amplitudes are not considered:

$$\hat{R}_\delta(\mathbf{x}_J, \omega) \approx \sum_n \delta(\mathbf{x}_J - \mathbf{x}_n). \tag{13}$$

In this expression, n is the index of the point-scatterer and $\mathbf{x}_n$ is its location. The Green's function $\hat{G}_\delta$ can be explained by a primary forward model, analogous to equation (6):

$$\hat{G}_\delta(\mathbf{x}_B, \mathbf{x}_A, \omega) \approx \int_{\mathbb{D}_A} \hat{W}_p^-(\mathbf{x}_B, \mathbf{x}_J, \omega)\, \hat{R}_\delta(\mathbf{x}_J, \omega)\, \hat{W}_p^+(\mathbf{x}_J, \mathbf{x}_A, \omega)\, \mathrm{d}^3\mathbf{x}_J. \tag{14}$$

We migrate the response $\hat{G}_\delta$, analogous to equation (7), that is

$$M_{G\delta}(\mathbf{x}'_J) = \int_\Omega \int_{\partial\mathbb{D}_A} \int_{\partial\mathbb{D}_A} \{\hat{W}_p^+(\mathbf{x}'_J, \mathbf{x}_B, \omega)\}^* \hat{G}_\delta(\mathbf{x}_B, \mathbf{x}_A, \omega) \times \{\hat{W}_p^-(\mathbf{x}_A, \mathbf{x}'_J, \omega)\}^* \mathrm{d}^2\mathbf{x}_A \mathrm{d}^2\mathbf{x}_B \mathrm{d}\omega. \tag{15}$$

In Fig. 8(b), we show the image $M_{G\delta}$ for the Sigsbee example with physical sources and receivers in the borehole. To interpret this result, we substitute equations (13) and (14) into equation (15), yielding:

$$M_{G\delta}(\mathbf{x}'_J) \approx \sum_n \int_\Omega \int_{\partial\mathbb{D}_A} \int_{\partial\mathbb{D}_A} \{\hat{W}_p^+(\mathbf{x}'_J, \mathbf{x}_B, \omega)\}^* \hat{W}_p^-(\mathbf{x}_B, \mathbf{x}_n, \omega) \times \{\hat{W}_p^+(\mathbf{x}_n, \mathbf{x}_A, \omega)\{\hat{W}_p^-(\mathbf{x}_A, \mathbf{x}'_J, \omega)\}^* \mathrm{d}^2\mathbf{x}_A \mathrm{d}^2\mathbf{x}_B \mathrm{d}\omega. \tag{16}$$

Or, with the help of equation (9):

$$M_{G\delta}(\mathbf{x}'_J) \approx \sum_n \int_\Omega \hat{\Gamma}_M(\mathbf{x}_n, \mathbf{x}'_J, \omega)\mathrm{d}\omega. \tag{17}$$

Thus, $M_{G\delta}$ can be interpreted as a superposition of blurred image points $\mathbf{x}_n$, where the blurring is quantified by $\hat{\Gamma}_M$. This type of image can be used to diagnose the illumination conditions in the image domain. In Fig. 8(b), the image points are relatively well focused, except at the edges of the image domain. Note that the image contains an additional imprint of the wavelet $\hat{S}$, since we used $\hat{P}_\delta$ instead of $\hat{G}_\delta$ for this analysis. In Fig. 8(b), we visualized the illumination of trial image points by physical sources in the borehole. Next, we will repeat this experiment for the interferometric data, generated from physical sources at the surface and virtual sources in the borehole.

To simulate how the trial image points would be illuminated by virtual sources, we convolve $\hat{G}_\delta$ with the interferometric point-spread functions that were observed from physical sources at the surface, analogous to equation (4):

$$\hat{C}_\delta(\mathbf{x}_B, \mathbf{x}'_A, \omega) = \int_{\partial\mathbb{D}_A} \hat{G}_\delta(\mathbf{x}_B, \mathbf{x}_A, \omega)\, \hat{\Gamma}_I(\mathbf{x}_A, \mathbf{x}'_A, \omega)\mathrm{d}^2\mathbf{x}_A. \tag{18}$$

The correlation function $\hat{C}_\delta$ is migrated, as in equation (10), yielding:

$$M_{C\delta}(\mathbf{x}'_J) = \int_\Omega \int_{\partial\mathbb{D}_A} \int_{\partial\mathbb{D}_A} \{\hat{W}_p^+(\mathbf{x}'_J, \mathbf{x}_B, \omega)\}^* \hat{C}_\delta(\mathbf{x}_B, \mathbf{x}'_A, \omega) \times \{\hat{W}_p^-(\mathbf{x}'_A, \mathbf{x}'_J, \omega)\}^* \mathrm{d}^2\mathbf{x}'_A \mathrm{d}^2\mathbf{x}_B \mathrm{d}\omega. \tag{19}$$

By substitution of equations (18), (13) and (14) into equation (19), it follows that:

$$M_{C\delta}(\mathbf{x}'_J) \approx \sum_n \int_\Omega \int_{\partial\mathbb{D}_A} \int_{\partial\mathbb{D}_A} \{\hat{W}_p^+(\mathbf{x}'_J, \mathbf{x}_B, \omega)\}^* \hat{W}_p^-(\mathbf{x}_B, \mathbf{x}_n, \omega) \times \left[\int_{\partial\mathbb{D}_A} \hat{W}_p^+(\mathbf{x}_n, \mathbf{x}_A, \omega)\hat{\Gamma}_I(\mathbf{x}_A, \mathbf{x}'_A, \omega)\mathrm{d}^2\mathbf{x}_A\right] \times \{\hat{W}_p^-(\mathbf{x}'_A, \mathbf{x}'_J, \omega)\}^* \mathrm{d}^2\mathbf{x}'_A \mathrm{d}^2\mathbf{x}_B \mathrm{d}\omega. \tag{20}$$

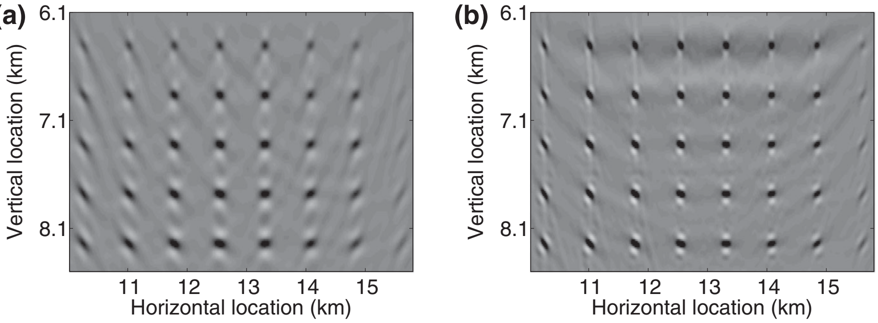

Figure 9 a) Image of the point scatterers obtained with virtual sources retrieved by a) cross-correlation and b) multidimensional deconvolution.

Or, with the help of equation (12):

$$M_{C\delta}(\mathbf{x}'_J) \approx \sum_n \int_\Omega \hat{\Gamma}_{IM}(\mathbf{x}_n, \mathbf{x}'_J, \omega)\mathrm{d}\omega. \quad (21)$$

Thus, $M_{C\delta}$ can be interpreted as a superposition of blurred trial image points, where the blurring is quantified by the interferometric migration point-spread function $\hat{\Gamma}_{IM}$. The constructed image $M_{C\delta}$ for the Sigsbee example (with illumination by virtual sources in the borehole, being constructed from physical sources at the surface) is shown in Fig. 9(a). Note that illuminating the image points with virtual sources results in stronger blurring than illuminating them with physical sources in the borehole. The image points at the right side of the grid in Fig. 9(a) have a stronger imprint than those at the left side, which is consistent with our observation that the right side of the borehole has been under-illuminated.

Finally, the effects of multidimensional deconvolution are analysed. For this purpose, we repeat the procedure with a point-spread function that is deconvolved by itself (with regularization). The result is shown in Fig. 9(b). Note that the imprint of $\hat{\Gamma}_I$ has been largely removed. As a result, the interferometric image has improved, as we have seen in Fig. 6.

In this example, the image points have been illuminated well, such that multidimensional deconvolution could be applied. This is not always the case. In some situations, the point-spread functions have strong directional imprints and cannot be inverted due to notches in the illuminated spectrum. The interferometric migration point-spread function can be used to analyse such directivity, see Loureiro *et al.* (2012) for an example. Alternatively, this imprint can be analysed by singular value decomposition of the matrix that defines convolution with the downgoing field in the forward problem of multidimensional deconvolution (equation (3)). Poor illumination leads to a large number of zeros among the singular values, making the inverse problem poorly conditioned, see Minato, Matsuoka and Tsuji (2013) for an illustration.

It should be emphasized that illumination diagnosis in the image domain can be carried out without velocity information from the overburden. We could replace the grid of point scatterers by any other object to analyse how such an object would be imaged by physical sources or virtual sources. Lecomte (2008) and Toxopeus *et al.* (2008) showed that seismic images can be simulated by filtering a geological model with the migration point-spread function. In a similar way, interferometric images can be simulated by filtering a geological model with the interferometric migration point-spread function.

A POINT-SPREAD FUNCTION FOR SIMULTANEOUS-SOURCE ACQUISITION

The last decade has seen an increasing popularity of simultaneous-source (or blended) acquisition (Berkhout 2008). Overlapping sources can decrease acquisition time (Hampson, Stefani and Herkenhoff 2008) and speed-up computational processes (Neelamani *et al.* 2010). Wapenaar, Van der Neut and Torbecke (2012) presented the following forward model for simultaneous-source acquisition:

$$\hat{U}_0(\mathbf{x}_B, \sigma_S^{(m)}, \omega) = \int_{\partial\mathbb{D}_A} \hat{G}_0(\mathbf{x}_B, \mathbf{x}_A, \omega)\hat{B}(\mathbf{x}_A, \sigma_S^{(m)}, \omega)\mathrm{d}^2\mathbf{x}_A. \quad (22)$$

In this representation, $\hat{U}_0(\mathbf{x}_B, \sigma_S^{(m)}, \omega)$ is the upgoing wavefield from a source group $\sigma_S^{(m)}$ that is recorded at $\mathbf{x}_B$, where both $\sigma_S^{(m)}$ and $\mathbf{x}_B$ are located at the earth's surface, which we define here as $\partial\mathbb{D}_A$. We assume that the medium has no free surface, which is indicated with subscript 0. In equation (22), $\hat{U}_0$ is described as a multidimensional convolution of the Green's function $\hat{G}_0$ $(\mathbf{x}_B, \mathbf{x}_A, \omega)$ with a single source

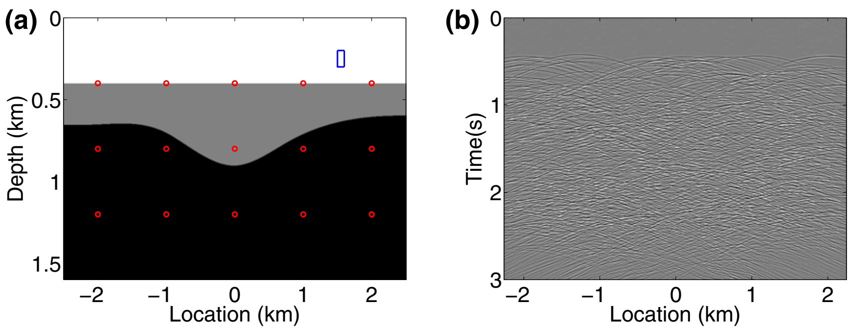

Figure 10 a) Density model for the synthetic example. The red circles denote trial image points and the blue rectangle denotes an area where passive locations are situated in a later example. b) Blended shot record, where 451 sources are fired simultaneously with excitation times varying randomly between 0–2 s.

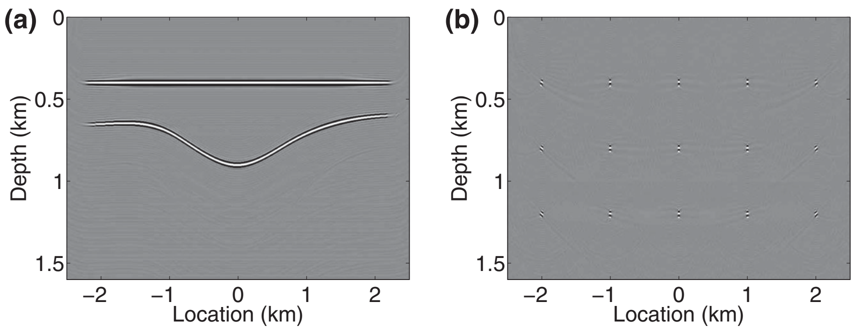

Figure 11 Image of a) the subsurface and b) the trial image points, obtained by sequential-source acquisition.

at $\mathbf{x}_A$ and a receiver at $\mathbf{x}_B$ (both located at the acquisition surface) with the blending function:

$$\hat{B}(\mathbf{x}_A, \sigma_S^{(m)}, \omega) = \sum_{a \in \sigma_S^{(m)}} \exp\left(-j\omega t^{(a)}\right)\delta(\mathbf{x}_A - \mathbf{x}_A^{(a)}). \tag{23}$$

Here, $\sigma_S^{(m)}$ denotes groups of simultaneous sources, with m being the source group number. Each source group contains several individual sources, indicated by index number a. Each individual source is fired at a specific location $\mathbf{x}_A^{(a)}$ with a specific delay time $t^{(a)}$. Wapenaar *et al.* (2012) showed that equation (22) is closely related to the forward model that we presented in equation (3). This can be easily verified by choosing $\partial\mathbb{D}_A$ in equation (3) just below the acquisition surface in a medium that is homogeneous above this surface, such that the downgoing field can be represented directly by the blending function. Following similar reasoning as we applied to equation (3), we find that normal equation (4) is satisfied, with the correlation function:

$$\hat{C}(\mathbf{x}_B, \mathbf{x}'_A, \omega) = \sum_m \hat{U}_0(\mathbf{x}_B, \sigma_S^{(m)}, \omega)\hat{B}^*(\mathbf{x}'_A, \sigma_S^{(m)}, \omega) \tag{24}$$

and the interferometric point-spread function:

$$\hat{\Gamma}_I(\mathbf{x}_A, \mathbf{x}'_A, \omega) = \sum_m \hat{B}(\mathbf{x}_A, \sigma_S^{(m)}, \omega)\hat{B}^*(\mathbf{x}'_A, \sigma_S^{(m)}, \omega). \tag{25}$$

The cross-correlated data $\hat{C}$ are often referred to as pseudo-deblended data (Mahdad, Doulgeris and Blacquière 2011). From equation (4), we can see that the pseudo-deblended data inherit an imprint of $\hat{\Gamma}_I$, causing undesired effects that are often referred to as cross-talk.

Normal equation (4) can be used to predict the cross-talk from simultaneous-source acquisition when pseudo-deblending is applied. We will illustrate this concept with a synthetic example. In Fig. 10(a), we show the density model, where the grey colour corresponds to 1500 kg/m^3 and the black colour to 2000 kg/m^3. For convenience, the velocity is kept constant at 2000 m/s. At the surface, 451 sources and 451 receivers are deployed with 10 m spacing. We model and migrate the data with conventional sequential-source acquisition, see Fig. 11(a). Next, we repeat the experiment for an extreme case of simultaneous-source acquisition by blending all 451 sources in a single record of 4 s, with excitation times varying randomly between 0–2 s. The blended shot record is shown in Fig. 10(b). We apply pseudo-deblending with equation (24) and migrate the result, see Fig. 12(a). Note that the cross-talk manifests itself mostly as background noise, whereas the two reflectors that exist in the model can still be recognized well.

Remember from equation (11) that the image in Fig. 12(a) should be interpreted as a convolution of the true reflectivity

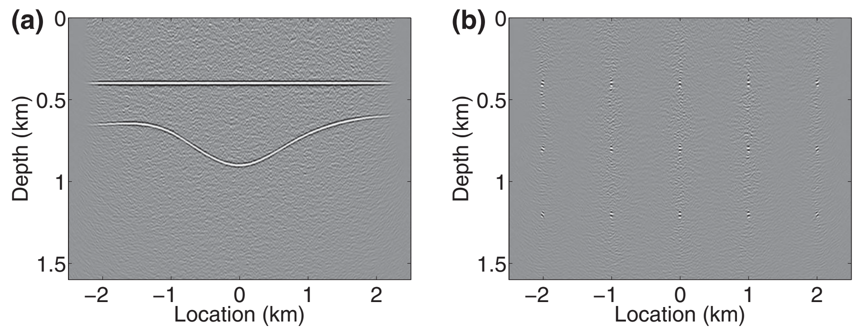

Figure 12 Image of a) the subsurface and b) the trial image points, obtained by simultaneous-source acquisition

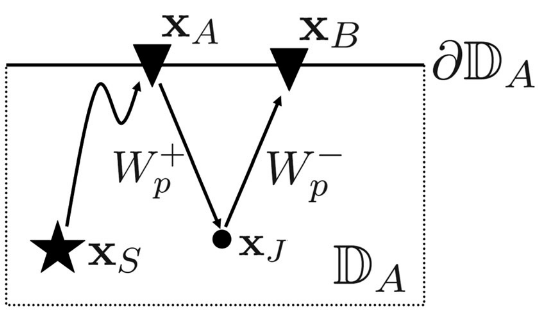

Figure 13 Configuration for passive interferometric imaging. Noise sources are located at $\mathbf{x}_S$ inside the volume $\mathbb{D}_A$. Receivers are located at $\mathbf{x}_A$ and $\mathbf{x}_B$ at the surface, where receiver $\mathbf{x}_A$ is transformed into a virtual source. The retrieved data are connected to the reflection operator R at image point $\mathbf{x}_J$ through the downward and upward propagators for primaries $W_p^{\pm}$.

with the interferometric migration point-spread functions. To visualize these point-spread functions, we model the reflection response from a grid of point scatterers that are indicated by red circles in Fig. 10(a), representing trial image points. An image of these point scatterers with sequential-source acquisition is shown in Fig. 11(b). This result should be interpreted as a superposition of the migration point-spread functions at the trial image points under sequential-source acquisition. We repeat the experiment but prior to migration we convolve the Green's functions with the point-spread functions for pseudo-deblending as computed with equation (25). The result, shown in Fig. 12(b), should be interpreted as a superposition of the interferometric migration point-spread functions at the trial image points under simultaneous-source acquisition. It is clear that the cross-talk produces incoherent noise above and below the image points, whereas the image points themselves are still properly focused.

To remove the imprint of the simultaneous-source acquisition is not trivial. One approach is to remove the cross-talk by prediction-and-subtraction (Mahdad *et al.* 2011). Alternatively, the forward problem can be inverted. Unfortunately, this inverse problem is underdetermined and additional sparseness or coherency constraints should be imposed to obtain a stable solution (Neelamani *et al.* 2010). In the special case where the source groups are small and contain adjacent, densely sampled sources, deblending can be implemented by least-squares inversion if an additional spatial filter is applied (Wapenaar *et al.* 2012b).

A POINT-SPREAD FUNCTION FOR PASSIVE SEISMIC INTERFEROMETRY

Claerbout (1968) showed that auto-correlating the transmission response at the surface of a single noise source below a set of reflectors in a 1D medium provides a 1D reflection response. Wapenaar and Fokkema (2006) generalized this concept. They derived that the reflection response of a 3D heterogeneous medium can be retrieved by cross-correlating surface recordings of simultaneously-acting uncorrelated noise sources in the subsurface. The theory has been tested numerically and has been applied to exploration-scale field data (Draganov *et al.* 2009). Others applied a similar methodology for imaging crustal-scale discontinuities (Poli, Campillo and Pedersen 2012). Several studies have pointed out that ambient noise fields are often directive, causing complications for Green's function retrieval (Weaver, Froment and Campillo 2009). Various correctional filters have been proposed to remove the imprint of non-isotropic source distributions, see Curtis and Halliday (2010) and Gallot *et al.* (2012) for examples.

Alternatively, passive interferometry can be interpreted as an inverse problem that can be solved by multidimensional deconvolution (Wapenaar, Van der Neut and Ruigrok 2008) or sparse inversion (Van Groenestijn and Verschuur 2010). The configuration for this problem is shown in Fig. 13. Unlike in conventional interferometric redatuming

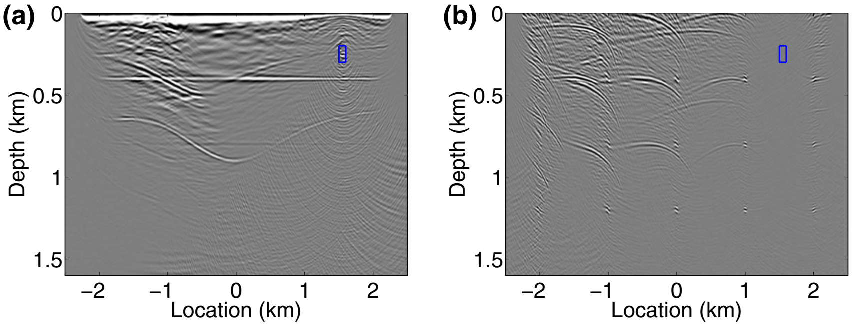

Figure 14 a) Image of the subsurface obtained by passive interferometry. b) Image of a grid of point scatterers when illuminated by virtual sources (obtained by passive interferometry in the physical medium).

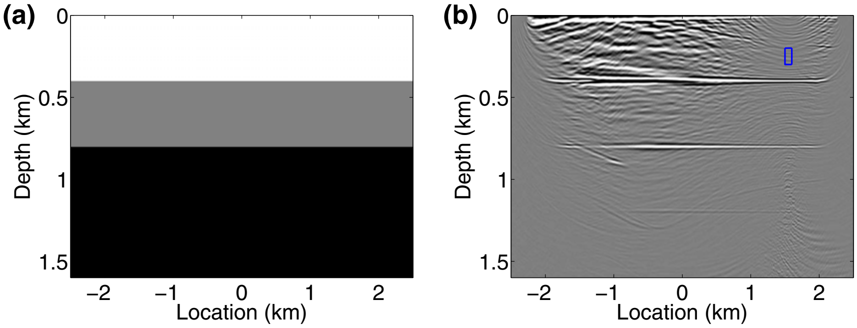

Figure 15 a) Reference medium with two horizontal reflectors. b) Image of the reference medium when illuminated by virtual sources (obtained by passive interferometry in the physical medium).

(see Fig. 1), the sources are located inside the integration volume $\mathbb{D}_A$. Moreover, the source locations are generally unknown, source signatures can be complex and sources can be acting simultaneously. To allow multidimensional deconvolution for this specific configuration, it is required to define a reference medium (indicated with subscript 0), which is identical to the physical medium, with the free surface replaced by a homogeneous half-space above $\partial\mathbb{D}_A$ (i.e., absorbing boundaries). Wapenaar *et al.* (2008) derived the following forward model for this situation:

$$\hat{V}(\mathbf{x}_B, \omega) - \hat{V}_0(\mathbf{x}_B, \omega) = \int_{\partial\mathbb{D}_A} \hat{G}_d(\mathbf{x}_B, \mathbf{x}_A, \omega)\, \hat{P}_0(\mathbf{x}_A, \omega)\, \mathrm{d}^2\mathbf{x}_A. \quad (26)$$

In this model, $\hat{V}(\mathbf{x}_B, \omega)$ is the recorded particle velocity response at sensor $\mathbf{x}_B$ at the earth's surface from a collection of noise sources in the subsurface, whereas $\hat{V}_0(\mathbf{x}_B, \omega)$ and $\hat{P}_0(\mathbf{x}_A, \omega)$ are the particle velocity and pressure responses that would be recorded in the absence of a free surface. Note that these fields are the result of an arbitrary selection of noise sources throughout the subsurface that may or may not be simultaneously acting with possibly complex signatures. Hence, the dependence on source location $\mathbf{x}_S$ can no longer be specified. Further, $\hat{G}_d(\mathbf{x}_B, \mathbf{x}_A)$ is the desired Green's function in a medium with a free surface, as if there were a dipole (indicated by subscript d) virtual source at $\mathbf{x}_A$ at the surface and a receiver at $\mathbf{x}_B$. The normal equation (4) is once more satisfied (where $\hat{G}_0$ should be replaced by $\hat{G}_d$), with the correlation function:

$$\hat{C}(\mathbf{x}_B, \mathbf{x}'_A, \omega) = [\hat{V}(\mathbf{x}_B, \omega) - \hat{V}_0(\mathbf{x}_B, \omega)]\, \hat{P}^*_0(\mathbf{x}'_A, \omega) \quad (27)$$

and the interferometric point-spread function:

$$\hat{\Gamma}_I(\mathbf{x}_A, \mathbf{x}'_A, \omega) = \hat{P}_0(\mathbf{x}_A, \omega)\, \hat{P}^*_0(\mathbf{x}'_A, \omega). \quad (28)$$

In practice, long ensemble averages of noise are evaluated to capture sufficient noise sources in the subsurface. The pressure response $\hat{P}_0$ can be estimated from $\hat{V}_0$ through $\hat{P}_0 \approx \hat{V}_0$ (where amplitude-versus angle characteristics are not preserved). However, in practice it is hard to estimate $\hat{V}_0$, since the data without free surface cannot be recorded. Wapenaar *et al.* (2008) suggested to separate $\hat{V}_0$ by time-gating the first arrivals in raw passive recordings. However, this approach cannot be applied if noise sources are acting simultaneously. For this reason, Van der Neut (2012) suggested to cross-correlate the full recordings $\hat{V}$ and to interpret the contributions around zero time-lag as $\hat{\Gamma}_I$ and the contributions at causal time-lags as $\hat{C}$. In this paper, we go one step further by interpreting the full cross-correlated wavefield both as $\hat{\Gamma}_I$ and $\hat{C}$. This means that inversion of normal equation (4) is no longer possible. This can easily be seen, since such an inversion would lead to a trivial solution $\hat{G}(\mathbf{x}_B, \mathbf{x}_A, \omega) = \hat{\delta}(\mathbf{x}_B - \mathbf{x}_A)$, being a Dirac delta function. However, this approach still

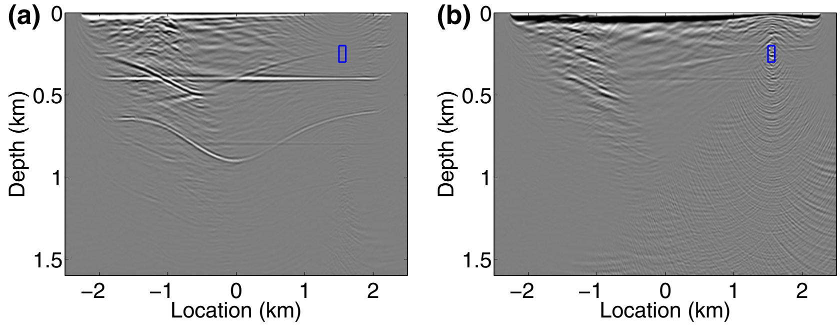

Figure 16 a) Image as in Fig. 15(b), where the physical medium (as in Fig. 10 a) is used as a reference medium. b) Result after subtracting the image in Fig. 16(a) from the image in Fig. 14(a).

allows us to analyse the interferometric migration point-spread function in the image domain in some situations.

To illustrate the use of the previous representations, we place 100 simultaneously acting noise sources that are active for 10 minutes in a local area of 100 m x 100 m, which is indicated by the blue box in Fig. 10(a). Finite-difference modelling is conducted with the help of a software package that was developed by Thorbecke and Draganov (2011). Data are collected at the surface, cross-correlated and migrated, yielding the image in Fig. 14(a). Note that no time-gating was applied. Hence, the cross-correlated data contain not only reflections stemming from correlations of $\hat{V}$ and $\hat{V}_0$ but also correlations of $\hat{V}_0$ and $\hat{V}_0$. Since the recording times are short and the sources are distributed very locally in this example, the interferometric image is far from perfect and various artefacts can be identified. Note for instance the ghost image of the lowest reflector, being caused by so-called spurious arrivals (Snieder *et al.* 2006).

We visualize the interferometric migration point-spread functions by convolving the retrieved data (representing the interferometric point-spread functions in this case) with the impulse response of a grid of point-scatterers (representing trial image points) that are indicated by the red circles in Fig. 10(a). The result is migrated, yielding the image in Fig. 14(b). We can clearly observe that the trial image points at positive horizontal locations surrounding the source area have been focused well, whereas the trial image points at negative horizontal locations are relatively defocused. Moreover, we observe several events surrounding the point-scatterers, giving rise to the spurious events that we observed before.

Figure 14(b) can be interpreted as an image of the point scatterers as they would be seen by passive interferometry under the given source distribution. We can replace the reflection response of the point scatterers with the reflection response of an arbitrary reference medium, for instance a medium with two horizontal reflectors as indicated in Fig. 15(a), and repeat the exercise. To do so, we model the response of the reference medium, convolve with the cross-correlated data from the noise sources and migrate the result, yielding the image in Fig. 15(b). This result should be interpreted as an image of the reference medium when illuminated by the passive sources. This type of analysis can provide insights into the artefacts to expect from any observed passive source distribution if Fig. 15(a) would be the subsurface model.

We repeat the experiment with the reflectors in the reference medium placed at their correct positions. That is, we compute reflection data in the physical medium with sources and receivers at the surface, convolve with the cross-correlated data from the passive sources and migrate. The result is shown in Fig. 16(a). Comparing Fig. 16(a) and Fig. 14(a), we clearly observe that various spurious events that obscure the interferometric image have been predicted well. However, various artefacts in Fig. 14(a) cannot be found in Fig. 16(a). This is especially clear when we subtract both images, see Fig. 16(b). All artefacts in this figure occur because the full wavefields have been correlated (including correlations of $\hat{V}_0$ and $\hat{V}_0$) and migrated, while the desired $\hat{C}$ should contain only correlations of $\hat{V}$ and $\hat{V}_0$. As such, the interferometric image in Fig. 14(a) should be interpreted as a superposition of the predicted artefacts in Fig. 16(a) and additional artefacts stemming from not separating $\hat{V}$ and $\hat{V}_0$.

The proposed analysis can provide insight into the accuracy of an interferometric image. Given any passive data set as observed in the field and a trial reflectivity model of the subsurface, artefacts in the interferometric image can be predicted and possibly identified to enhance interpretation. Potentially, the interferometric image can be improved by removing the point-spread function with multidimensional deconvolution but this is not always a trivial excercise, especially not if contributions of $\hat{V}$ and $\hat{V}_0$ cannot be separated well.

CONCLUSION

With seismic interferometry, a physical receiver can be effectively transformed into a virtual source, either by cross-correlation or by multidimensional deconvolution. A virtual source can radiate either downwards or upwards, depending on the type of waves that are cross-correlated or deconvolved. Interferometric imaging is defined as sequentially applying seismic interferometry and imaging. We showed that an interferometric image can contain artefacts that are effectively described by the interferometric migration point-spread function. We showed how this function can be visualized and how spurious events in the interferometric image can be predicted in cases where an estimate of the subsurface reflectivity is available. The interferometric image can be improved by applying multidimensional deconvolution prior to imaging. However, this approach is not always feasible in practice. Alternatively, we may deconvolve the interferometric migration point-spread function in the image domain. The formulations in this paper may provide useful forward models to do so in the future. Although these formulations have been inspired by acquisition systems with downhole receivers, the required Green's functions for interferometric redatuming can also be modelled or obtained with an iterative scheme that is currently being developed (so-called Marchenko redatuming). Also for these scenarios, the point-spread functions that are described in this paper can be used for an image-domain diagnosis (and potentially removal) of artefacts caused by internal multiples from the overburden.

ACKNOWLEDGEMENTS

This research is supported by the Dutch Technology Foundation STW, applied science division of NWO and the Dutch Technology Program of the Ministry of Economic Affairs. We thank Jan Thorbecke (Delft University of Technology), Felix Herrmann and Tristan van Leeuwen (University of British Columbia) for collaboration.

REFERENCES

Amundsen L. 2001. Elimination of free-surface related multiples without need of the source wavelet. *Geophysics* **66**, 327–341.

Bakulin A. and Calvert R. 2006. The virtual source method: Theory and case study. *Geophysics* **71**, SI139–SI150.

Bakulin A., Mateeva A., Calvert R., Jorgensen P. and Lopez J. 2007a. Virtual shear source makes shear waves with air guns. *Geophysics* **72**, A7–A11.

Bakulin A., Mateeva A., Mehta K., Jorgensen P., Ferrandis J., Sinha Herhold I. and Lopez J. 2007b. Virtual source applications to imaging and reservoir monitoring. *The Leading Edge* **26**, 732–740.

Berkhout A.J. 1997. Pushing the limits of seismic imaging, Part I: Prestack migration in terms of double dynamic focusing. *Geophysics* **62**, 937–953.

Berkhout A.J. 2008. Changing the mindset in seismic data acquisition. *The Leading Eedge* **27**, 924–938.

Berkhout A.J. and Wapenaar C.P.A. 1993. A unified approach to acoustical reflection imaging II: The inverse problem. *Journal of the Acoustical Society of America* **93**, 2017–2023.

Berryhill J.R. 1984. Wave-equation datuming before stack. *Geophysics* **49**, 2064–2066.

Bharadwaj P., Schuster G.T., Mallinson I. and Dai W. 2011. Theory of supervirtual refraction interferometry. *Geophysical Journal International* **188**, 263–273.

Biondi B. 2010. Velocity estimation by image-focusing analysis. *Geophysics* **75**, U49–U60.

Brand E., Hurich C. and Deemer D. 2013. Geometrical considerations in the acquisition of borehole interferometric data for imaging near-vertical features: Design of field experiments. *Geophysics* **78**, K1–K10.

Broggini F., Snieder R. and Wapenaar K. 2012. Focusing the wavefield inside an unknown 1D medium: Beyond seismic interferometry. *Geophysics* **77**, A25–A28.

Byun J., Yu J. and Seol S.J. 2010. Crosswell monitoring using virtual sources and horizontal wells. *Geophysics* **75**, 37–43.

Chavarria J.A., Goertz A., Karrenbach M., Paulsson B., Milligan P., Soutyrine V. *et al*. 2007. The use of VSP techniques for fault characterization: An example from the San Andreas Fault. *The Leading Edge* **26**, 770–776.

Claerbout J.F. 1968. Synthesis of a layered medium from its acoustic transmission response. *Geophysics* **33**, 264–269.

Curtis A. and Halliday D. 2010. Source-receiver wavefield interferometry. *Physical Review E* **81**, 046601.

De Bruin C.G.M., Wapenaar C.P.A. and Berkhout A.J. 1990. Angle-dependent reflectivity by means of prestack migration. *Geophysics* **55**, 1223–1234.

Del Molino G., Andreoletti C., Sandroni S., Poletto F., Petronio L., Farina B. et al. 2011. Seismic interferometry application to improve seismic reflection signals affected by ice-plate flexural noise. *The Leading Edge* **30**, 538–545.

Dong S., Sheng J. and Schuster G.T. 2006. Theory and practice of refraction interferometry. 76th Annual Meeting, SEG, Expanded Abstracts, 3021–3025.

Draganov D., Campman X., Thorbecke J., Verdel A. and Wapenaar K. 2009. Reflection images from ambient seismic noise. *Geophysics* **74**, A63–A67.

Draganov D., Ghose R., Ruigrok E., Thorbecke J. and Wapenaar K. 2010. Seismic interferometry, intrinsic losses and Q-estimation. *Geophysical Prospecting* **58**, 361–373.

Forghani F. and Snieder R. 2010. Underestimation of body waves and feasibility of surface-wave reconstruction by seismic interferometry. *The Leading Edge* **29**, 790–794.

Gaiser J.E. and Vasconcelos I. 2010. Elastic interferometry for ocean bottom cable data: Theory and examples. *Geophysical Prospecting* **58**, 347–360.

Gaiser J., Vasconcelos I., Geetan R. and Faragher J. 2012. Elastic-wavefield interferometry using P-wave source VSPs, Wamsutter field, Wyoming. *Geophysics* 77, Q27–Q36.

Gallot T., Catheline S., Roux P. and Campillo M. 2012. A passive inverse filter for Green's function retrieval. *Journal of the Acoustical Society of America* **131**, EL21–EL27.

Halliday D.F., Curtis A., Robertsson J.O.A. and Van Manen D.J. 2007. Interferometric surface-wave isolation and removal. *Geophysics* **72**, A69–A73.

Hampson G., Stefani J. and Herkenhoff F. 2008. Acquisition using simultaneous sources. *The Leading Edge* **27**, 918–923.

Hanafy S.M. and Schuster G.T. 2014. Interferometric interpolation of sparse marine data. *Geophysics* **62**, 1–16.

He R., Karrenbach M., Paulsson B. and Soutyrine V. 2009. Near-wellbore VSP imaging without overburden. *Geophysics* **74**, SI9–SI14.

Hornby B.E. and Yu J. 2007. Interferometric imaging of a salt flank using walkaway VSP data. *The Leading Edge* **26**, 760–763.

King S. and Curtis A. 2012. Suppressing nonphysical reflections in Green's function estimates using source-receiver interferometry. *Geophysics* **77**, Q15–Q25.

King S., Curtis A. and Poole T.L. 2011. Interferometric velocity analysis using physical and nonphysical energy. *Geophysics* **76**, SA35–SA49.

Konstantaki L.A., Draganov D., Heimovaara T. and Ghose R. 2013. Imaging scatterers in landfills using seismic interferometry. *Geophysics* **78**, EN107–EN116.

Lecomte I. 2008. Resolution and illumination analyses in PSDM: A ray-based approach. *The Leading Edge* **27**, 650–663.

Loureiro A., Van der Neut J., Alves D., Carvalho J., Afilhado A., Draganov D. *et al*. 2012. Estimation of imageable dip range of target structures in interferometric salt flank imaging with limited illumination. 74^{th} EAGE Conference and Exhibition, Extended Abstracts, X003.

Mahdad A., Doulgeris P. and Blacquière G. 2011. Separation of blended data by iterative estimation and subtraction of blending interference noise. *Geophysics* **76**, Q9–Q17.

Mehta K., Bakulin A., Sheiman J., Calvert R. and Snieder R. 2007. Improving the virtual source method by wavefield separation. *Geophysics* **72**, V79–V86.

Mehta K., Kiyashchenko D., Jorgensen P., Lopez J., Ferrandis J. and Costello M. 2010. Virtual source method applied to crosswell and horizontal well geometries. *The Leading Edge* **29**, 712–723.

Mehta K., Sheiman J.L., Snieder R. and Calvert R. 2008. Strengthening the virtual-source method for time-lapse monitoring. *Geophysics* **73**, S73–S80.

Menke W. 1989. *Geophysical Data Aanalysis*. Academic Press.

Mikesell T.D., Van Wijk K., Calvert A. and Haney M.M. 2009. The virtual refraction: Useful spurious energy in seismic interferometry. *Geophysics* **74**, A13–A17.

Minato S., Matsuoka T. and Tsuji T. 2013. Singular-value decomposition analysis of source illumination in seismic interferometry by multidimensional deconvolution. *Geophysics* **78**, Q25–Q34.

Minato S., Matsuoka T., Tsuji T., Draganov D., Hunziker J. and Wapenaar K. 2011. Seismic interferometry using multidimensional deconvolution and crosscorrelation for crosswell seismic reflection data without borehole sources. *Geophysics* **76**, SA19–SA34.

Neelamani R., Krohn C.E., Krebs J.R., Romberg J.K., Deffenbaugh M. and Anderson J.E. 2010. Efficient seismic forward modeling using simultaneous random sources and sparsity. *Geophysics* **75**, WB15–WB27.

Paffenholz J., McLain B., Zaske J. and Keliher P. 2002. Subsalt multiple attenuation and imaging: Observations from the Sigsbee2B synthetic dataset. 72^{nd} Annual Meeting, SEG, Expanded Abstracts, 2122–2125.

Plessix R.E. and Mulder W.A. 2004. Frequency-domain finite-difference amplitude-preserving migration. *Geophysical Journal International* **157**, 975–987.

Poli P., Campillo M. and Pedersen H. 2012. Body-wave imaging of the Earth's mantle discontinuities from ambient seismic noise. *Science* **338**, 1063–1065.

Poliannikov O.V. 2011. Retrieving reflections by source-receiver wavefield interferometry. *Geophysics*, **76**, SA1–SA8.

Poliannikov O.V., Rodenay S. and Chen L. 2012. Interferometric imaging of the underside of a subducting crust. *Geophysical Journal International* **189**, 681–690.

Poliannikov O.V. and Willis M.E. 2011. Interferometric correlogram-space analysis. *Geophysics* **76**, SA9–SA17.

Ramírez A.C. and Weglein A.B. 2009. Green's theorem as a comprehensive framework for data reconstruction, regularization, wavefield separation, seismic interferometry, and wavelet estimation: A tutorial. *Geophysics* **74**, W35–W62.

Ruigrok E., Campman X. and Wapenaar K. 2011. Extraction of P-wave reflections from microseisms. *Comptes Rendus Geoscience* **343**, 512–525.

Schuster G.T. 2009. *Seismic Interferometry*. Cambridge University Press.

Schuster G.T. and Hu J. 2000. Green's function for migration: Continuous recording geometry. *Geophysics* **65**, 167–175.

Schuster G.T. and Zhou M. 2006. A theoretical overview of model-based and correlation-based redatuming methods. *Geophysics* **71**, SI103–SI110.

Snieder R., Wapenaar K. and Larner K. 2006. Spurious multiples in seismic interferometry of primaries. *Geophysics* **71**, SI111–SI124.

Tao Y. and Sen M.K. 2013. On a plane-wave based crosscorrelation-type seismic interferometry. *Geophysics* **78**, Q35–Q44.

Tatanova M., Mehta K. and Kashtan B. 2009. Applications of virtual refraction in time-lapse monitoring. 79^{th} Annual Meeting, SEG, Expanded Abstracts, 2617–2621.

Thorbecke J. 1997. *Common focus point technology*. PhD thesis, Delft University of Technology.

Thorbecke J. and Wapenaar K. 2007. On the relation between seismic interferometry and the migration resolution function. *Geophysics* **72**, T61–T66.

Thorbecke J. W. and Draganov D. 2011. Finite-difference modeling experiments for seismic interferometry. *Geophysics* **76**, H1–H18.

Thorbecke J.W., Wapenaar K. and Swinnen G. 2004. Design of one-way wavefield extrapolation operators using smooth functions in WLSQ optimization. *Geophysics* **69**, 1037–1045.

Toxopeus G., Thorbecke J., Wapenaar K., Petersen S., Slob E. and Fokkema J. 2008. Simulating migrated and inverted seismic data by filtering a geological model. *Geophysics* **73**, T1–T10.

Van der Neut J. 2012. *Interferometric redatuming by multidimensional deconvolution*. PhD thesis, Delft University of Technology.

Van der Neut J. and Herrmann F.J. 2013. Interferometric redatuming by sparse inversion. *Geophysical Journal International* **192**, 666–670.

Van der Neut J., Thorbecke J., Mehta K., Slob E. and Wapenaar K. 2011. Controlled-source interferometric redatuming by crosscorrelation and multidimensional deconvolution in elastic media. *Geophysics* **76**, SA63–SA76.

Van Groenestijn G.J.A. and Verschuur D.J. 2010. Estimation of primaries by sparse inversion from passive seismic data. *Geophysics* **75**, SA61–SA69.

Vasconcelos I. and Rickett J. 2013. Broadband extended images by joint inversion of multiple blended wavefields. *Geophysics* **78**, WA147–WA158.

Vasconcelos I. and Snieder R. 2008. Interferometry by deconvolution, Part I: Theory for acoustic waves and numerical examples. *Geophysics* **73**, S115–S128.

Vasconcelos I., Snieder R. and Hornby B. 2008. Imaging internal multiples from subsalt VSP data – Examples of target-oriented interferometry. *Geophysics* **73**, S157–S168.

Wang Y., Dong S. and Luo Y. 2010. Model-based interferometric interpolation method. *Geophysics* **75**, WB211–WB217.

Wang Y., Luo Y. and Schuster G.T. 2009. Interferometric interpolation of missing seismic data. *Geophysics* **74**, SI37–SI45.

Wapenaar K. 2006. Green's function retrieval by cross-correlation in case of one-sided illumination. *Geophysical Research Letters* **33**, L19304.

Wapenaar C.P.A. and Berkhout A.J. 1993. Representations of seismic reflection data, Part I: State of affairs. *Journal of Seismic Exploration* **2**, 123–131.

Wapenaar K., Broggini F. and Snieder R. 2012a. Creating a virtual source inside a medium from reflection data: Heuristic derivation and stationary-phase analysis. *Geophysical Journal International* **190**, 1020–1024.

Wapenaar K. and Fokkema J. 2006. Green's function representations for seismic interferometry. *Geophysics* **71**, SI33–SI46.

Wapenaar K., Van der Neut J. and Ruigrok E. 2008. Passive seismic interferometry by multidimensional deconvolution. *Geophysics* **73**, A51–A56.

Wapenaar K., Van der Neut J., Ruigrok E., Draganov D., Hunziker J., Slob E. *et al.* 2011. Seismic interferometry by crosscorrelation and by multidimensional deconvolution: A systematic comparison. *Geophysical Journal International* **185**, 1335–1364.

Wapenaar K., Van der Neut J. and Thorbecke J. 2012 On the relation between seismic interferometry and the simultaneous-source method. *Geophysical Prospecting* **60**, 802–823.

Weaver R., Froment B. and Campillo M. 2009. On the correlation of non-isotropically distributed ballistic scalar diffuse waves. *Journal of the Acoustical Society of America* **126**, 1817–1826.

Willis M.E., Lu R., Campman X., Toksöz M.N., Zhang Y. and de Hoop M.V. 2006. A novel application of time-reversed acoustics: Salt-dome flank imaging using walkaway VSP surveys. *Geophysics* **71**, A7–A11.

Zheng Y. 2010. Retrieving the exact Green's function by wavefield crosscorrelation. *Journal of the Acoustical Society of America* **127**, EL93–EL98.